

Probabilistic Particle Flow Algorithm for High Occupancy Environment

A. Elagin^a, P. Murat^b, A. Pranko^c, A. Safonov^a

^a*Texas A&M University, College Station, TX 77843*

^b*Fermi National Accelerator Laboratory, Batavia, IL 60506*

^c*Ernest Orlando Lawrence Berkeley National Laboratory, Berkeley, CA 94720*

Abstract

Algorithms based on the particle flow approach are becoming increasingly utilized in collider experiments due to their superior jet energy and missing energy resolution compared to the traditional calorimeter-based measurements. Such methods have been shown to work well in environments with low occupancy of particles per unit of calorimeter granularity. However, at higher instantaneous luminosity or in detectors with coarse calorimeter segmentation, the overlaps of calorimeter energy deposits from charged and neutral particles significantly complicate particle energy reconstruction, reducing the overall energy resolution of the method. We present a technique designed to resolve overlapping energy deposits of spatially close particles using a statistically consistent probabilistic procedure. The technique is nearly free of ad-hoc corrections, improves energy resolution, and provides new important handles that can improve the sensitivity of physics analyses: the uncertainty of the jet energy on an event-by-event basis and the estimate of the probability of a given particle hypothesis for a given detector response. When applied to the reconstruction of hadronic jets produced in the decays of tau leptons using the CDF-II detector at Fermilab, the method has demonstrated reliable and robust performance.

1. Introduction to the Particle Flow Algorithm

Accurate measurement of the energy of hadronic jets is critical for precision verification of the Standard Model (SM) as well as searches for new physics

11 at current and future collider experiments. A standard jet energy measure-
 12 ment technique relies on clustering spatially close energy depositions in the
 13 calorimeter, the detector designed to measure the energy of particles that pro-
 14 duce electromagnetic or hadronic showers in the absorber material. Given that
 15 on average about 70% of a typical jet energy is carried by particles interacting
 16 hadronically¹ (mostly π^\pm , but also K^\pm , K_L^0 , protons, neutrons), the resolu-
 17 tion of the jet energy measurement is driven by the accuracy of the hadronic
 18 shower energy reconstruction. While the energy of electromagnetic showers
 19 can be measured very well, large fluctuations in the development of hadronic
 20 showers lead to a significantly lower precision². The non-equal response of the
 21 non-compensating calorimeters to electromagnetic and hadronic showers³ fur-
 22 ther biases the overall jet energy scale and degrades the resolution. Special
 23 corrections accounting for non-equal response can only partially recover this re-
 24 duction in resolution. While the presence of many particles in a jet averages
 25 out fluctuations in the measurement of energy of individual hadronic showers,
 26 jet energy resolution remains poor for jets of low (~ 10 – 30 GeV) and moderate
 27 (~ 30 – 60 GeV) energies. Incidentally, the resolution of low-to-moderate energy
 28 jets has a strong impact on the sensitivity of many physics analyses performed
 29 at hadron colliders, from precision measurements of the Standard Model pa-
 30 rameters to searches for the Higgs boson in $b\bar{b}$ and $\tau\tau$ channels and searches
 31 for new phenomena such as predicted by Supersymmetry. Mismeasurements of
 32 the jet energy also bias the measurement of the missing transverse energy (\cancel{E}_T)
 33 in an event, a key discriminant used in many analyses searching for new phe-
 34 nomena, calculated as an imbalance of the energy in the event in the direction
 35 transverse to the beam line. Enhancing the discovery potential of current and

¹the remaining 30% is mainly due to neutral pions decaying to pairs of photons, which produce electromagnetic showers.

²A typical example is the CDF calorimeter, which has good electromagnetic calorimeter resolution $\delta E/E \sim 0.135/\sqrt{E}$ while the response to stable hadrons, e.g. charged pions, is substantially less precise $\delta E/E \sim 0.5/\sqrt{E}$.

³E.g., main calorimeter systems at ATLAS, CDF, and CMS are all non-compensating.

future collider experiments is therefore motivating the development of improved jet energy measurement techniques.

A significant improvement in the jet energy resolution at hadron collider experiments has been achieved with the deployment of a technique known as the Particle Flow Algorithm (PFA), e.g. see [7]. PFA achieves better jet energy resolution by reconstructing and measuring energies of individual particles in a jet using information from several detector sub-systems. For example, the momenta of charged hadrons can be measured much more accurately using the tracking system (except for the case of very high transverse momenta, which is not relevant for this discussion), than in the calorimeter. This allows one to replace the less accurate calorimeter measurement of the energy carried by charged hadrons in the PFA jet energy calculation with:

$$E_{jet} = \sum_{tracks} E_{trk} + \sum_{\gamma's} E_{\gamma} + \sum_n E_n, \quad (1)$$

where the first term is the energy of the charged particles in the jet, the second term accounts for energy of photons accurately measured in the electromagnetic calorimeter, and E_n is the energy of stable neutral hadrons, e.g. neutrons or K_L^0 's, which still relies on the hadron calorimeter. The corresponding relative jet energy resolution can be written in terms of single particle relative resolutions as:

$$\frac{\sigma^2(E_{jet})}{E_{jet}^2} = \frac{1}{E_{jet}^2} \times \left(\sum_{tracks} E_{trk}^2 \frac{\sigma^2(E_{trk})}{E_{trk}^2} + \sum_{\gamma's} E_{\gamma}^2 \frac{\sigma^2(E_{\gamma})}{E_{\gamma}^2} + \sum_{n's} E_n^2 \frac{\sigma^2(E_n)}{E_n^2} \right) \quad (2)$$

Note that only the last term depends on the potentially poor calorimeter resolution for the energy of hadronic showers. However, because the fraction of the jet energy carried by stable neutral hadrons is on average only around 10%, its contribution to the overall jet energy uncertainty is strongly suppressed by $\sum E_n/E_{jet}$. With the remaining 90% of energy accurately measured either in the tracker or in the electromagnetic calorimeter, the PFA-based jet energy reconstruction can substantially outperform the traditional calorimeter-only based measurements. Furthermore, the bias in the energy scale related to calorime-

62 ter non-compensation effects is significantly reduced as it is only present in the
63 suppressed third term.

64 Apart from an obvious pre-requisite of highly efficient tracking, the perfor-
65 mance of a PFA-based reconstruction in a realistic setting depends critically on
66 one’s ability to correctly identify and separate calorimeter energy depositions
67 from spatially close particles. One example illustrating the issue is an overlap
68 of energy deposits in the calorimeter due to a charged pion and a neutron. In
69 this case one has to “guess” the fraction of the measured calorimeter energy
70 deposited by the charged pion, so that the excess can be attributed to a neutral
71 hadron. The dependence of the jet energy resolution on the overlap effects is
72 sometimes parameterized by amending Eq. (2) with the so called “confusion
73 term” [1] σ_{conf}^2 . The relative importance of the confusion term depends on the
74 power of the algorithm and the detector design features, but it generally in-
75 creases with the coarser calorimeter segmentation and higher particle densities.
76 In extreme cases, the large size of the confusion term can completely eliminate
77 the advantages of the PFA over traditional calorimeter-based measurements.

78 PF-based algorithms were successfully implemented at LEP in the 1990’s [2]
79 and have been pursued in developing the physics program at the International
80 Linear Collider (ILC) [3]. At hadron collider experiments, a simplified version of
81 a PFA-based algorithm was implemented for the reconstruction of hadronically
82 decaying tau leptons at CDF at the end of Run I [4]. In hadronic decays, a tau
83 lepton decays into a neutrino and one or more charged and neutral hadrons⁴.
84 While tau decays often proceed via intermediate resonances, e.g. ρ or a_1 , the
85 final stable charged hadrons are usually pions and, less often, kaons. Neutral
86 hadrons produced in hadronic tau lepton decays are dominated by neutral pi-
87 ons⁵, which promptly decay to photons via $\pi^0 \rightarrow \gamma\gamma$. Tau leptons accessible at
88 hadron machines typically originate from Z or W decays and therefore have

⁴the number of charged hadrons in tau lepton decays is always odd owing to the conserva-
tion of electric charge

⁵Only about 2% of the time tau decay products contain one or more neutral kaon

89 a substantial momentum. This leads to their decay products being fairly col-
 90 limated and appearing as jets of charged and neutral hadrons, reminiscent of
 91 regular jets originating from quarks or gluons. The decay products of tau lep-
 92 tons undergoing hadronic decays are therefore frequently referred to as “tau
 93 jets”. The PF-based reconstruction allowed for a strong improvement in the
 94 energy resolution of hadronic tau jets, and the technique was further improved
 95 and used at CDF for Run II analyses [5]. A more comprehensive implementation
 96 of the same technique [6] has been shown to improve the generic jet resolution
 97 at CDF compared to a calorimeter only reconstruction. However, the coarse
 98 segmentation of the CDF calorimeter has led to a sizable confusion term as-
 99 sociated with the substantial probability for more than one particle to deposit
 100 energy in a given calorimeter cluster. The difficulty in resolving such overlaps of
 101 energy depositions required to reconstruct momenta of individual particles al-
 102 lowed for only a limited improvement. A complete PFA algorithm developed by
 103 the CMS experiment [7] has allowed for a strong improvement in the jet energy
 104 measurement as well as a more accurate missing transverse energy scale and
 105 resolution. The CMS detector is well suited for PFA-based reconstruction due
 106 to the fine granularity of the electromagnetic calorimeter and the longitudinal
 107 profiling of hadronic showers in the central part of the detector, which improves
 108 their spatial resolution. However, the series of the “High Luminosity LHC”
 109 upgrades are expected to result in significant increases in particle occupancies
 110 per event. Maintaining high performance of the PFA-based reconstruction in
 111 the new regime requires the development of techniques capable of efficiently
 112 resolving energy overlaps.

113 In this paper, we discuss the challenges and implications of deploying a PFA-
 114 based reconstruction in an environment with frequent energy overlaps (Section
 115 2). In Section 3 we present a technique designed to resolve the overlapping
 116 energy depositions of spatially close particles using a statistically consistent
 117 probabilistic procedure. In addition to improving the energy resolution, the
 118 technique allows for combining measurements from multiple detectors, as op-
 119 posed to “substituting” one measurement with another in existing algorithms.

120 It is nearly free of ad-hoc corrections, thus minimizing distortions due to the
 121 discontinuities of the correction functions. The algorithm has additional unique
 122 features, such as the ability to calculate the jet energy uncertainty on a jet-by-jet
 123 basis, and provides the measure of the overall consistency of the measurement,
 124 improving the sensitivity of physics analyses. In Section 4, we describe the
 125 implementation of this technique for reconstructing the energy of tau jets, the
 126 decay products of hadronically decaying tau leptons, at CDF and illustrate its
 127 performance in a realistic setting using the actual experimental data in Section
 128 5.

129 **2. Challenges of the High Occupancy Environment**

130 The reconstruction of hadronically decaying tau jets at CDF is a good exam-
 131 ple of a problem with frequent overlaps of energy deposits from nearby particles.
 132 The CDF calorimeter has projective tower geometry with azimuthal segmenta-
 133 tion $\phi = 15^\circ$ and pseudorapidity segmentation $\eta \approx 0.1$ and provides very limited
 134 information about the lateral and longitudinal shower profiles⁶. With a typical
 135 angular size of a hadronic tau jet being of the order of 0.05-0.1 rad, there is
 136 a substantial probability for several or even all particles within the tau jet to
 137 cross the face of the calorimeter within the boundaries of a single calorimeter
 138 tower. Treatment of frequent energy overlaps is therefore a key consideration in
 139 designing a PFA-based reconstruction at CDF.

140 To set the stage, we need to briefly describe the sub-detector systems used in
 141 tau reconstruction and identification, a full description of the CDF-II detector is
 142 available elsewhere [8]. The CDF tracking system provides nearly 100% efficient
 143 tracking within the pseudorapidity range of $|\eta| < 1$, which is relevant for tau
 144 reconstruction. Its main element is the Central Outer Tracker (COT), a drift

⁶As discussed further in the text, there is a strip-wire chamber embedded inside the electro-
 magnetic calorimeter at $\sim 6X_0$, which allows for rough measurements of the lateral profile
 in some cases. Longitudinal profile information is limited to two energy measurements for
 deposits in the electromagnetic and hadron compartments of a tower.

145 chamber that covers radii from 0.4 m to 1.37 m immersed in a 1.4 T magnetic
 146 field, providing momentum resolution of $\delta p_T/p_T^2 \approx 0.0017(\text{GeV}/c)^{-1}$. If avail-
 147 able, hits from the silicon vertex detector (SVX) are added to the COT infor-
 148 mation, further improving the resolution. Central electromagnetic (CEM) and
 149 hadronic (CHA) calorimeters cover the pseudorapidity region of $|\eta| < 1.1$. CEM
 150 is a lead-scintillator calorimeter with resolution $\delta E_T/E_T = 0.135/\sqrt{E_T} \oplus 0.02$.
 151 CHA is an iron-scintillator calorimeter with the single pion energy resolution
 152 of $0.5/\sqrt{E_T} \oplus 0.03$. Both calorimeters have a projective tower geometry with
 153 tower size $\Delta\phi \times \Delta\eta \approx 15^\circ \times 0.1$ and neither of the calorimeters measures ei-
 154 ther the longitudinal or lateral shower profile. The Shower Maximum (CES)
 155 detector, consisting of a set of strip-wire chambers embedded inside the CEM
 156 at the expected maximum of the electromagnetic shower profile, enables mea-
 157 surement of the position of electromagnetic showers with an accuracy of a few
 158 mm by reconstructing clusters formed by strip and wires. While rarely used
 159 to measure energy of the electromagnetic showers, CES cluster's pulse height
 160 provides a measurement of electromagnetic shower energy with the resolution of
 161 $\delta E/E = 0.23$ for showers due to energetic photons or electrons. As pulse heights
 162 of the one-dimensional strip and wire clusters reconstructed for the same shower
 163 are typically within $\approx 7\%$ of each other⁷, multiple showers within a single CES
 164 chamber can typically be correctly reconstructed by matching the 1D strip and
 165 wire clusters using their pulse heights. The much broader hadronic showers
 166 frequently extend over multiple CHA towers and their spatial position can only
 167 be inferred from the energy measured in each tower. Early hadronic showers
 168 can deposit part of their energy in CEM and produce signals in CES, which
 169 sometimes complicates the reconstruction of CES clusters, e.g. if overlapping
 170 with showers produced by photons (from $\pi^0 \rightarrow \gamma\gamma$) in the same jet.

171 Let us consider a relatively simple example of a jet containing a charged

⁷The CES energy resolution is driven by the fluctuations in the amount of ionization produced inside the CES chambers and not by the measurement of the charge collected on strips and wires

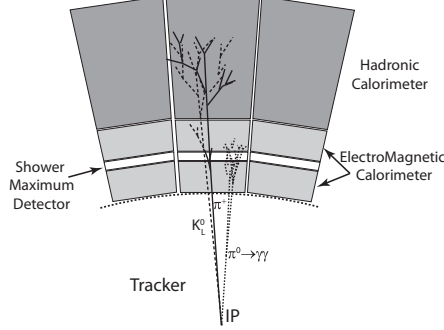


Figure 1: Illustration of the measurements available in the CDF-II detector setup for a hypothetical narrow jet of particles consisting of a charged pion (trajectory and the shower shown as solid lines), a neutral pion (dotted line) decaying to two unresolved photons and a neutral hadron (dashed line).

172 pion π^+ , a neutral pion π^0 decaying to two unresolved photons $\gamma_1\gamma_2$ (depositing
 173 energy in a single tower), and possibly a neutral hadron n , as illustrated in Fig. 1.
 174 While the π^+ momentum is known from the tracker, the energy estimation for
 175 neutral particles relies on the calorimeter measurement. However, the energy
 176 registered in the electromagnetic and hadronic parts of the calorimeter, E_{meas}^{EM}
 177 and E_{meas}^{HAD} , is a sum of the unknown deposits by each of the particles in the jet,
 178 including that by the charged pion:

$$E_{meas}^{EM} = E_{\pi^+}^{EM} + E_{\gamma_1\gamma_2}^{EM} + E_n^{EM} \quad (3)$$

$$E_{meas}^{HAD} = E_{\pi^+}^{HAD} + (E_{\gamma_1\gamma_2}^{HAD}) + E_n^{HAD}, \quad (4)$$

179 resulting in an under-constrained system with two equations and six unknowns.
 180 As the leakage of the electromagnetic showers from photons into the hadron
 181 calorimeter is typically small, as illustrated in Fig. 2(a) showing E^{EM} vs. E^{HAD}
 182 for simulated electrons, the corresponding term $E_{\gamma_1\gamma_2}^{HAD}$, shown in parentheses
 183 in Eq.(4), can be neglected. While it reduces the number of unknowns, solving
 184 the system of Eqs. (3,4) requires disentangling contributions from hadronically
 185 interacting particles. While $E_{\pi^+}^{EM}$ and $E_{\pi^+}^{HAD}$ terms are correlated with the ac-
 186 curately measured momentum of π^+ , the correlation is not trivial, as illustrated

187 in Fig. 2(b) showing the 2D distribution of E^{EM} vs. E^{HAD} for a simulated
 188 sample of charged pions with $p_{\pi^+} = 25$ GeV/c. The complex shape of the de-
 189 pendence owes to the large fluctuations in the development of hadronic showers
 190 and the non-compensating nature of the CDF calorimeter. As $E_{\pi^+}^{EM}$ cannot be
 191 reliably estimated, and E_n^{EM} is completely unconstrained, the momentum of the
 192 π^0 cannot be calculated directly. Estimating the jet energy directly in the PFA
 193 approach is therefore hampered by two issues: (i) difficulty in estimating E^{EM}
 194 for hadronically interacting particles, required to evaluate the π^0 momentum,
 195 and (ii) difficulty in estimating $E_{\pi^+}^{HAD}$, required to estimate the momentum of
 196 n . Measuring the momentum of a combined $\pi^0 + n$ system, e.g. by “guessing”
 197 the charged pion energy depositions and assigning the rest to the $\pi^0 + n$ system,
 198 is nearly exactly equivalent to measuring the jet energy using the calorimeter
 199 only thus negating all advantages of the PFA technique.

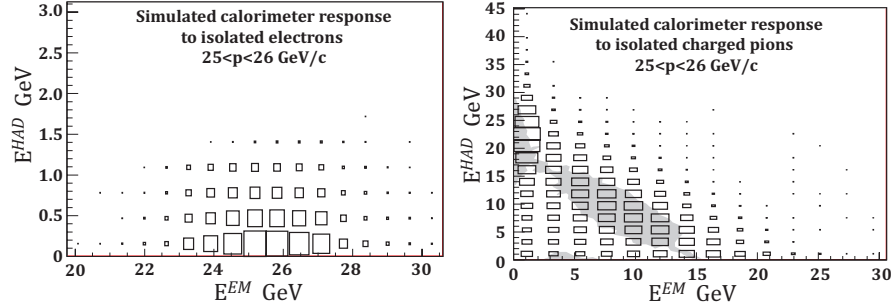


Figure 2: Examples of the calorimeter response for (a) simulated isolated electrons with $p = 25$ GeV/c and (b) simulated isolated charged pions with $p = 25$ GeV/c in the plane E^{EM} versus E^{HAD} . The size of the boxes in the plots is proportional to the probability density; the shaded area indicates the area of the highest density as obtained from the same distribution plotted with finer bin size.

200 An algorithm based on solving Eqs.(3,4) directly with the specific purpose
 201 of reconstructing hadronic tau jets was implemented in the “tracks+ π^0 ’s” algo-
 202 rithm at CDF and used in the early Run-II analyses. The idea was to simplify
 203 the problem by assuming the absence of neutral hadrons and estimate $E_{\pi^+}^{EM}$

204 as an average energy deposition in the EM calorimeter for a charged pion with
 205 given momentum (measured in the tracker). The remaining portion of the
 206 measured electromagnetic energy can then be taken as the energy of the π^0
 207 (Eq.(3)). Alternatively, one can assume that charged pions always behave in
 208 the electromagnetic calorimeter as minimal ionizing particles. While delivering
 209 a significant improvement over the calorimeter-only measurement for a large
 210 fraction of events, the algorithm featured long tails in the energy resolution.
 211 These tails have been traced to jets with several particles depositing energy in
 212 the same calorimeter tower. In physics analyses, an underestimation of the en-
 213 ergy of quark or gluon jets containing neutral hadronically interacting particles
 214 also leads to an increase in background contamination. Additional corrections
 215 based on detecting incompatibilities of the reconstructed energy with the ini-
 216 tially unused Eq.(4) or gross disagreements with the low resolution measurement
 217 of π^0 energy in the Shower Maximum detector allow for a reduction of the tails
 218 in the energy resolution. However, the ad-hoc nature and complexity of the
 219 corrections, as well as the algorithm's inability to consistently treat correlations
 220 and incorporate other available measurements motivate developing a more com-
 221 prehensive method.

222 **3. PPFA: The Probabilistic Particle Flow Algorithm**

223 The challenge of solving an underconstrained system with significant cor-
 224 relations and additional redundant measurements outlined in previous section
 225 can be addressed with a probabilistic approach. For every hypothesis of the jet
 226 particle content (the number of particles of each type), one can define a proba-
 227 bility estimator (likelihood) for a set of particles of given type and momenta to
 228 result in a particular set of detector measurements. These measurements could
 229 represent energy counts in calorimeter towers, cluster energies, track momenta
 230 or any other available measurement. The likelihood can be written as follows:

$$\mathcal{L}(\vec{p} | \vec{E}_{meas}) = \int \mathcal{M}(E_1^1, \dots, E_{i_p}^{j_m}, E_{meas}^1, \dots, E_{meas}^{j_m}) \times \prod_{i,j} \mathcal{P}_{ij}(E_i^j | p_i) dE_i^j, \quad (5)$$

231 where index i runs over particles in a jet ($i = 1, \dots, i_p$), p_i is the true momentum
 232 of particle i , E_{meas}^j stands for each available measurement ($j = 1, \dots, j_m$ runs
 233 over all available measurements), $\mathcal{P}_{ij}(E_i^j|p_i)$ is the “response function” for par-
 234 ticle i with true momentum p_i , to produce a contribution E_i^j to a measurement
 235 j (if the particle cannot contribute to the particular measurement j' , we use
 236 $\mathcal{P}_{ij'}(E_i^{j'}|p_i) = \delta(E_i^{j'})$), and \mathcal{M} contains information about correlations between
 237 contributions of each particle to each measurement. One example of the lat-
 238 ter is the correlation between the deposits of energy E_i^j in an electromagnetic
 239 calorimeter tower j by all particles crossing it, in which case \mathcal{M} will contain a
 240 product of expressions of the form $\delta(\sum_i E_i^j - E_{meas}^j)$ for each relevant tower j .
 241 The summation runs over all particles i that cross this tower and the delta func-
 242 tion ensures that the integration is performed over the parameter space where
 243 the assumed contributions to the measured energy by individual particles sum
 244 up into the experimentally measured energy deposition in that tower. Another
 245 example is the correlation between the energy deposited by particle i in the elec-
 246 tromagnetic calorimeter tower j_1 and a hadron calorimeter tower j_2 it crosses.
 247 In this case \mathcal{M} would have to account for the correlation between the energy
 248 deposits $E_i^{j_1}$ and $E_i^{j_2}$ in the two towers. Once such a global likelihood function
 249 is constructed, \bar{p}^0 corresponding to its maximum will determine the most prob-
 250 able set of particle momenta, thus achieving the goal of fully reconstructing the
 251 event using all available detector information. The type of each particle and
 252 their number can be taken as parameters of the global likelihood, allowing one
 253 to also determine the most probable particle content of a jet.

254 While building a global and fully inclusive likelihood is certainly possible,
 255 it is hardly practical. However, this approach can be deployed to solve spe-
 256 cific problems like measuring jet energies in environments with frequent energy
 257 overlaps in the calorimeter. Here, we will describe an example of one such pos-
 258 sible PPFA implementation. For simplicity, this example will use the energy of
 259 pre-reconstructed electromagnetic and hadronic calorimeter clusters as the basic
 260 measurements E_{meas}^j , but an implementation using tower energy measurements

would be very similar. The PPFA probability for a set of particles with momenta p_i to produce a set of calorimeter measurements E_{meas}^j for each cluster j in electromagnetic or hadron calorimeter can be written as follows:

$$\mathcal{L}_p(\vec{p}|\vec{E}_{meas}) = \int \mathcal{M}' \prod_j \delta(\sum_i E_i^j - E_{meas}^j) \times \prod_{i,j} \mathcal{P}_{ij}(E_i^j|p_i) dE_i^j, \quad (6)$$

where \vec{p} is the vector of particle momenta p_i , index i runs over the list of particles in a jet, index j runs over the available measurements (in our example, the electromagnetic and hadronic calorimeter's cluster energy measurements), E_i^j is the contribution to the measured energy in cluster j by i^{th} particle, E_{meas}^j is the measured energy for cluster j , and the response function $\mathcal{P}_{ij}(E_i^j|p_i)$ is the probability for particle i with true momentum p_i to deposit energy E_i^j in cluster j (\mathcal{P}_{ij} depends on the type of particle), and \mathcal{M}' describes correlations that remain unaccounted after the delta functions have been introduced. The likelihood \mathcal{L}_p is essentially a sum of probabilities of all possible outcomes, i.e. the specific values of energy deposited by each particle in the electromagnetic and hadronic calorimeter clusters, consistent with the actual cluster energy measurements (the latter is ensured by the delta functions). The probability of each outcome is a product of probabilities \mathcal{P}_{ij} for each particle to deposit given amounts of energy $E_i^{j_1}$, $E_i^{j_2}$ in the hadronic and electromagnetic calorimeters, given their assumed true momenta p_i . In many practical cases, the strongest effect that \mathcal{M}' in Eq.(6) has to properly account for is the correlation of the values of the deposits by the same particle in the electromagnetic and hadronic calorimeters, e.g. early showering of a charged hadron can lead to a larger than typical deposition of energy in the electromagnetic calorimeter, but the energy deposited in the hadron calorimeter would consequently be lower than typical. The easiest way to take this kind of correlation into account is to switch to two-dimensional response functions $\mathcal{P}^{CAL}(E_i^{EM_{j_1}}, E_i^{HAD_{j_2}}|p_i)$, where j_1 and j_2 are the indices of the electromagnetic and hadronic calorimeter clusters the particle traverses. In this case, \mathcal{M}' is no longer needed and the distributions shown in Figs. 2(a) and (b) can be normalized and used as response functions $\mathcal{P}^{CAL}(E^{EM}, E^{HAD}|p)$ for electrons and charged pions, respectively. For numerical calculations in practi-

cal applications, one should first simplify the expression for \mathcal{L}_p by integrating over some of the variables to remove delta functions. In some cases it is as easy as dropping the integration over dE_i^j with the combinations of indices i and j corresponding to cases where particle i is making no contribution to measurement j , which is equivalent to integrating over the corresponding dE_i^j and taking into account that $\mathcal{P}_{ij}(E_i^j|p_i) = \delta(E_i^j)$ in the above equation. In other cases, one needs to choose which variables to integrate over to optimize the speed and accuracy of the numeric calculations.

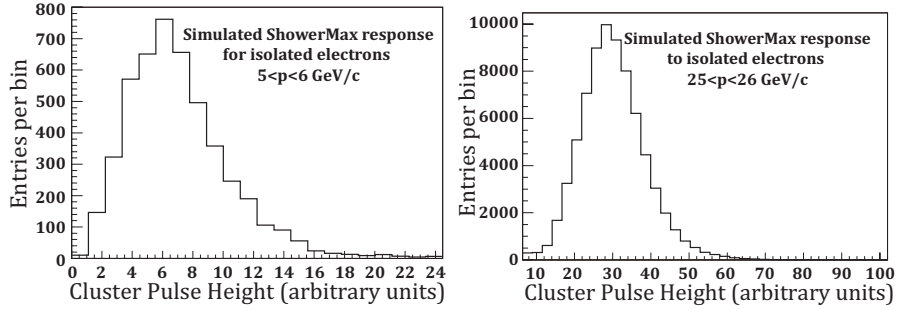


Figure 3: Examples of the Shower Maximum detector response functions for simulated isolated electrons with momenta in the ranges $p = 5 - 6$ GeV/c (left) and $p = 25 - 26$ GeV/c (right). Similarity in the response between electrons and photons allows using these functions in constructing likelihood functions for either electrons or photons.

Additional measurements can be easily incorporated by modifying the likelihood function with Bayesian-like “priors”. For example, information from tracking or Shower Maximum detectors can be added by multiplying the initial likelihood function by a probability to measure a certain track momentum or pulse height given the assumed true momentum of charged pions, electrons or photons. For example, distribution shown in Fig. 3 upon normalization can be used as the response functions of the Shower Maximum detector $\mathcal{P}_\gamma^{CES}(E^{CES}|p_\gamma)$ for photons with momenta ranges $p = 5 - 6$ and $25 - 26$ GeV/c. The inclusion of “priors” is equivalent to expanding the list of measurements in the original likelihood function and introducing further correlation information into the matrix

308 \mathcal{M} .

309 While the most probable set of particle momenta \vec{p}^0 is obtained by maximiz-
 310 ing the likelihood $\mathcal{L}_p(\vec{p}|\vec{E}_{meas})$, the likelihood shape in the \vec{p} space can be used
 311 to evaluate the uncertainty in the energy determination for each particle. If one
 312 primarily seeks to measure the energy of a particular jet in the event as often
 313 is the case, one can use the likelihood defined in Eq.(6) to obtain a “posterior”
 314 distribution for the jet energy, defined as a sum of the energies of the particles
 315 assigned to the jet. This is accomplished by integrating over $d\vec{p} = dp_1 \dots dp_{i_p}$

$$\mathcal{L}_E(E_{jet}|\vec{E}_{meas}) = \int \mathcal{L}_p(\vec{p}|\vec{E}_{meas}) \times \delta(\sum_{i=1}^N p_i - E_{jet}) d\vec{p}, \quad (7)$$

316 and we have assumed here that the first N particles in the list are those assigned
 317 to the jet in question. In the presence of correlations, \mathcal{L}_E may provide a more
 318 convenient estimate of the jet energy and its uncertainty. The shape of the jet
 319 energy “posterior” allows for the estimation of the uncertainty in the measured
 320 jet energy. If one needs to simultaneously evaluate the energy of several jets in
 321 the event, Eq.(7) needs to be modified by introducing additional delta-functions
 322 (one per jet) with the summation running over indices of particles assigned to
 323 each of the jets.

324 Once the most likely set of particle momenta \vec{p}^0 is found, one can further
 325 test the “goodness” of the particle hypothesis. We define a p-value as the
 326 probability to observe a combination of detector measurements \vec{E}'_{meas} that is
 327 equally or less likely than the actual set \vec{E}_{meas} observed in the event, given that
 328 the true combination of particles and momenta is the one that maximizes the
 329 likelihood in Eq. (6):

$$p(\vec{p}^0, \vec{E}_{meas}) = \frac{\int_{\mathcal{L}_p(\vec{p}^0|\vec{E}'_{meas}) \leq \mathcal{L}_p(\vec{p}^0|\vec{E}_{meas})} \mathcal{L}_p(\vec{p}^0|\vec{E}'_{meas}) d\vec{E}'_{meas}}{\int \mathcal{L}_p(\vec{p}^0|\vec{E}'_{meas}) d\vec{E}'_{meas}} \quad (8)$$

330 The p-value can be easily calculated numerically by generating “pseudo-experi-
 331 ments,” in which one generates “pseudo-deposits” of energy by each particle
 332 with momenta p_i^0 towards each cluster energy measurement using the same re-
 333 sponse functions. The sum of the deposits of all particles crossing particular

clusters yields a set of pseudo-measurements \vec{E}'_{meas} . The probability of the generated outcome is given by \mathcal{L}_p , and the integrated probability of observing equally or less probable set of measurements than the actually observed \vec{E}_{meas} gives the p-value. A too low p-value may indicate that the initial particle hypothesis should be modified. Note that interpreting measured p-values has to be done carefully as the arbitrary addition of new particles to make the observed calorimeter response “perfect” may degrade the resolution by biasing the measurement towards the calorimeter-based jet energy measurement. While the p-value defined in Eq.(8) is global for the entire event, a p-value can be defined for each individual jet or a set of particles. For example, one can either build \mathcal{L}_p by only include particles of interest, e.g. the ones belonging to a particular jet, or by integrating the global \mathcal{L}_p over a subset of momenta p_i belonging to particles that are of no interest for a given measurement.

4. PPFA-Based Reconstruction of Hadronically Decaying Tau Leptons at CDF

In this section we describe a practical implementation of the method developed for hadronic tau jet reconstruction at CDF. In the following, we discuss the CDF baseline hadronic tau jet reconstruction, which is used as a starting point for the algorithm. We then discuss the PPFA strategy, measurement of the response functions, mathematical definition of the PPFA likelihood function and the “p-value,” and the algorithm used for correcting the initial particle hypothesis. We conclude with evaluating the algorithm’s energy resolution using simulation. As we are primarily interested in improving energy reconstruction for tau jets, we implement a “local” version of the PPFA, with the definitions presented in the previous section only including particle candidates that contribute to a particular jet and completely ignoring the rest of the information contained in the event.

361 4.1. Baseline Hadronic Tau Jet Reconstruction at CDF

362 The construction of hadronic tau jet candidates at CDF starts with select-
363 ing continuous clusters of calorimeter towers. The clustering starts with a “seed
364 tower,” defined as any tower with $E_T > 5$ GeV/c and at least one track with
365 $p_T > 5$ GeV/c pointing to the cluster. Broad clusters with more than six con-
366 tiguous calorimeter towers with $E_T > 1$ GeV/c are excluded from consideration
367 as true tau jets almost always result in narrow clusters of just a few towers.
368 Clusters outside the central part of the detector ($|\eta| \leq 1$) are also discarded to
369 ensure a high tracking efficiency for the remaining candidates. Given the size
370 of the CDF calorimeter towers of $\Delta\eta \times \Delta\phi \sim 0.1 \times 0.25$, the efficiency of the
371 calorimeter-related selections is very high, reaching nearly 100% for hadroni-
372 cally decaying taus with visible $p_T > 10$ GeV/c. The seed track p_T requirement
373 brings a non-negligible inefficiency for tau jets of low-to-moderate visible mo-
374 mentum, but its strong power in rejecting quark and gluon jet backgrounds
375 made it a standard in all CDF analyses involving hadronic tau jets. Next, all
376 tracks within a signal cone of $\Delta R = \sqrt{\Delta\phi^2 + \Delta\eta^2} < 0.17$ around the seed track
377 are associated with the tau candidate.

378 4.2. Implementation Strategy

379 The likelihood-based PPFA algorithm starts with the initial hypothesis that
380 every reconstructed track is a charged pion, every reconstructed cluster in the
381 Shower Maximum detector with no track pointing to it is a photon, and no other
382 particles are present in the jet. While this initial hypothesis can be corrected at
383 a later point in the algorithm, in most cases it turns out to be true owing to the
384 low rate of the track and Shower Maximum reconstruction failures and the low
385 branching fraction of hadronic tau lepton decays for modes with neutral hadrons
386 except π^0 's, e.g. $\tau \rightarrow K_L + X$. Next, we define the probability function using
387 pre-calculated response functions (details for both are discussed in the following
388 two sub-sections) and perform a scan in the multi-dimensional parameter space
389 of momenta of the particles, assumed to comprise the hadronic tau jet, searching
390 for the maximum of the likelihood function.

391 After the most likely combination of particle momenta is determined, we
 392 construct the “p-value” which measures the probability that the given parti-
 393 cle content and momenta hypothesis result in detector measurements less or
 394 equally as likely as the observed response. If the p-value is too low, the particle
 395 content hypothesis is modified by adding a photon, which is assumed to be not
 396 reconstructed either due to the detector inefficiency or an overlap with a track
 397 (Shower Maximum cluster will be vetoed if it is reconstructed too close to the
 398 extrapolated position of a charged track), and the full calculation is repeated. If
 399 the p-value remains too low, the particle content is modified by adding a stable
 400 neutral hadron (K_L) and the likelihood calculation is repeated. The procedure
 401 continues until an acceptable outcome is achieved or after running out of the
 402 pre-set options.

403 *4.3. Response Functions of the CDF Detector Sub-systems*

404 As discussed earlier, the relevant detector measurements include tracking,
 405 measurements of energy deposited in the electromagnetic and hadronic calorime-
 406 ter towers, and the measured CES cluster energy. Because the precision of the
 407 CDF tracking is much higher than the accuracy of other measurements, the
 408 tracker response function for charged pions as a function of pion momenta can
 409 be safely approximated by a delta function to simplify further calculations. To
 410 determine the calorimeter response functions for charged pions, we use the CDF
 411 GEANT-3 [9] based simulation package tuned using the test beam data. Iso-
 412 lated charged pions are selected using hadronic tau decays $\tau^\pm \rightarrow \pi^\pm \nu_\tau$ from an
 413 inclusive $Z/\gamma^* \rightarrow \tau\tau$ simulated sample of events generated with Pythia [10]. We
 414 calculate response functions for charged pions with momenta ranging from 1
 415 to 100 GeV/c in steps of 1 GeV/c. Large fluctuations in the development of
 416 hadronic showers and their large lateral size, frequently spanning across several
 417 CHA towers, make it impractical to calculate responses separately for each tower
 418 in a multi-tower cluster. Instead, we measure the hadronic calorimeter response
 419 for charged pions by summing tower energies in a square of 3×3 towers centered
 420 on the extrapolated position of the π^\pm track. In the CEM, hadronic showers

rarely deposit energy in more than a single tower, therefore the charged pion
 electromagnetic deposition is calculated using the energy in the tower pointed
 at by the track associated with π^\pm . To take into account the strong correlation
 of the energy depositions by the same particle in CEM and CHA, we define
 a 2-dimensional response function in the E^{EM} versus E^{HAD} plane. Fig. 2(b)
 shows an example of the calorimeter responses in CEM and CHA for simulated
 isolated charged pions with momenta $25 < p_\pi < 26$ GeV/c. The adequacy of the
 CDF simulation of the calorimeter response can be inferred from the results of
 a dedicated study [12], in which simulation predictions were compared with the
 pion test beam data and with the collisions data using a pure sample of isolated
 charged pions. When normalized to unity, these response functions represent
 the probability density functions (PDF) for a charged pion with a particular
 momentum to produce a given response in the calorimeter, which we will refer
 to as $\mathcal{P}_\pi^{CAL}(E^{EM}, E^{HAD}|p_\pi)$.

The vast majority of photons in tau jets originate from $\pi^0 \rightarrow \gamma\gamma$ and typi-
 cally have energy of the order of a few GeV, making accurate understanding of
 the calorimeter response for low energy photons particularly important. While
 the response functions for photons can be measured directly from the simu-
 lation, validating them with the data can be difficult owing to the challenges
 in selecting a high purity sample of low energy photons in data. Fortunately,
 the calorimeter response to photons and electrons is nearly identical, allowing
 for the use of a relatively high purity sample of electrons in data obtained by
 tagging photon conversions. Similar to the case of charged pions, we calculate
 2-dimensional response functions for photons with momenta ranging from 1 to
 100 GeV/c in steps of 1 GeV/c in the E^{EM} versus E^{HAD} plane. Fig. 2(a) shows
 an example of the calorimeter response function for photons with the true mo-
 menta $25 < p_\gamma < 26$ GeV/c. We denote the response functions of this type as
 $\mathcal{P}_\gamma^{CAL}(E^{EM}, E^{HAD}|p_\gamma)$.

As mentioned earlier, the CES energy measurement is used in the likelihood
 function as, despite its modest resolution, it can help correctly assign energies
 in difficult cases. As photon candidates reconstructed in CES have highly cor-

related strip and wire pulse heights, we only use the strip based measurements to determine the energy of a given CES cluster. Examples of the CES response functions $\mathcal{P}_\gamma^{CES}(E^{CES}|p_\gamma)$ for isolated photons with energies $5 < p_\gamma < 6$ GeV and $25 < p_\gamma < 26$ GeV are shown in Figs. 3(a) and (b), respectively.

4.4. Computation of the PPFA Likelihood

In our implementation, the initial particle hypothesis assumes each reconstructed track to be due to a charged pion and each reconstructed CES cluster not associated with a track to be due to a photon (or perhaps two merged photons, which makes little difference). The tracking momentum measurement is taken to be exact due to the superior resolution of the CDF tracker. To include calorimeter measurements, the highest p_T track associated to a tau candidate is extrapolated to the CES radius and the corresponding calorimeter tower becomes a seed tower. A grid of 3x3 towers is formed around the seed tower, and each track and CES cluster is associated to one tower on the grid. Each electromagnetic tower provides its own measurement \vec{E}_{meas}^{EM} (components of this vector will be denoted as $E_{meas}^{EM_j}$ $j = 1, \dots, 9$) used in the likelihood. For the hadronic calorimeter, we sum the energies of all nine towers into a single measurement, $E_{meas}^{HAD} = \sum E_{meas}^{HAD_j}$, for the entire "super-cluster". Under the assumption that the decay products of a tau jet are charged tracks and photons, the likelihood function has the following form:

$$\begin{aligned} \mathcal{L}_p(\vec{p}_\pi, \vec{p}_\gamma, \vec{p}_n | \vec{E}_{meas}^{EM}, E_{meas}^{HAD}, \vec{E}_{meas}^{CES}) = \\ \int \delta\left(\sum_{i=1}^{N_\gamma} E_{\gamma_i}^{HAD} + \sum_{k=1}^{N_\pi} E_{\pi_k}^{HAD} + \sum_{l=1}^{N_n} E_{n_l}^{HAD} - E_{meas}^{HAD}\right) \times \\ \prod_{j=1}^9 dE_{\gamma_i}^{EM_j} dE_{\pi_k}^{EM_j} dE_{n_l}^{EM_j} \delta\left(\sum_{i=1}^{N_\gamma} E_{\gamma_i}^{EM_j} + \sum_{k=1}^{N_\pi} E_{\pi_k}^{EM_j} + \sum_{l=1}^{N_n} E_{n_l}^{EM_j} - E_{meas}^{EM_j}\right) \times \\ \prod_{i=1}^{N_\gamma} dE_{\gamma_i}^{HAD} \prod_{k=1}^{N_\pi} dE_{\pi_k}^{HAD} \prod_{l=1}^{N_n} dE_{n_l}^{HAD} \mathcal{P}_\gamma^{CAL}(E_{\gamma_i}^{EM_j}, E_{\gamma_i}^{HAD} | p_{\gamma_i}) \times \\ \mathcal{P}_\pi^{CAL}(E_{\pi_k}^{EM_j}, E_{\pi_k}^{HAD} | p_{\pi_k}) \mathcal{P}_n^{CAL}(E_{n_l}^{EM_j}, E_{n_l}^{HAD} | p_{n_l}) \mathcal{P}_\gamma^{CES}(E_{\gamma_i}^{CES} | p_{\gamma_i}), \quad (9) \end{aligned}$$

where the integration runs over all possible depositions of energy by each individual particle in each available calorimeter measurement, the delta functions in the second line ensure that the sum of the deposits for each measurement is equal to the observed value, and the third line includes response functions for photons, charged pions and neutral hadrons in the calorimeter and in the CES detector. One can choose to convert Eq.(9) into a posterior probability distribution to estimate the hadronic tau jet energy as:

$$\mathcal{L}_E(E_{jet}|\vec{E}_{meas}^{EM}, E_{meas}^{HAD}, \vec{E}_{meas}^{CES}) = \int \mathcal{L}_p(\vec{p}_\pi, \vec{p}_\gamma|\vec{E}_{meas}^{EM}, E_{meas}^{HAD}, \vec{E}_{meas}^{CES}) \times \delta\left(\sum_{i=1}^{N_\gamma} p_{\gamma_i} + \sum_{k=1}^{N_\pi} p_{\pi_k} + \sum_{l=1}^{N_n} p_{n_l} - E_{jet}\right) d\vec{p}_\pi d\vec{p}_\gamma d\vec{p}_n \quad (10)$$

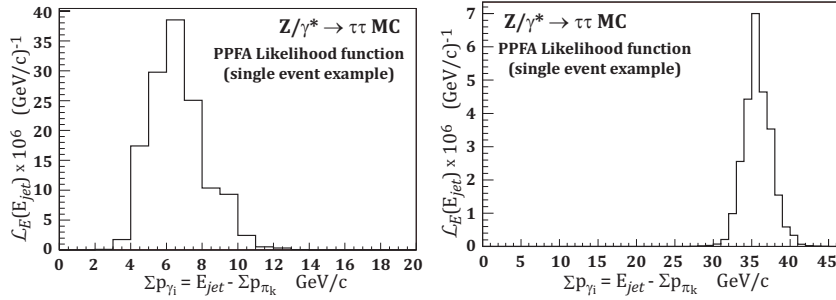


Figure 4: Examples of $\mathcal{L}_E(E_{jet})$ for two representative simulated $Z \rightarrow \tau\tau$ events plotted versus combined energy of the photon candidates in the jet related to E_{jet} via $\sum p_\gamma = E_{jet} - \sum p_\pi$. These distributions serve as statistical probability density functions for the values of the measured energy for a given jet. In the PPFA implementation discussed in this paper, the maximum of the $\mathcal{L}_E(E_{jet})$ distribution is used as the estimator for the jet energy, while the width and the shape of the distribution yield the uncertainty in the measurement of the jet energy on a jet-by-jet basis.

While the integral form presented in Eqs.(9,10) appears fairly complicated, it is straightforward to implement in the code and compute numerically using the Monte Carlo integration technique. Values of \vec{p}_{π_k} and \vec{p}_{γ_i} , which maximize $\mathcal{L}(\vec{p}_\pi, \vec{p}_\gamma)$ in Eq.(9) represent the best estimate for energies of particles produced in the tau decay, under the assumption that the initial hypothesis about the par-

484 ticle content was correct. Figure 4 shows examples of the $\mathcal{L}_E(E_{jet})$ distributions
 485 for two representative events from a sample of simulated $Z \rightarrow \tau\tau$ events.

486 4.5. The Reduced p-Value Definition

487 Photon reconstruction failures or the presence of a stable neutral hadron,
 488 e.g. K_L^0 , may lead to an incorrect initial particle hypothesis. Such occurrences
 489 result in a suboptimal estimation of the energy, and therefore it is important to
 490 detect and correct such cases. We define a p-value using Eq.(8), but, to speed up
 491 the calculations, we do two simplifications to the definition of the likelihood \mathcal{L}_p
 492 in Eq. (9). First, because in practice most of the cases affected by the incorrect
 493 initial hypothesis can be identified through inconsistencies between the avail-
 494 able calorimeter and tracker measurements, we drop the terms associated with
 495 the CES. Second, we combine the nine electromagnetic towers in the hadronic
 496 tau cluster into a single “super-tower” with energy $E^{EM} = \sum E^{EM_j}$, where
 497 the summation runs over the nine towers, and define the “reduced” version of
 498 Eq. (9):

$$\begin{aligned} \mathcal{L}'_p(\vec{p} | (E_{meas}^{EM}, E_{meas}^{HAD})) &= \int \delta\left(\sum_{m=1}^9 E_{meas}^{EM_m} - E_{meas}^{EM}\right) \\ &\times \mathcal{L}_p(\vec{p} | \vec{E}_{meas}^{EM}, E_{meas}^{HAD}) \prod_{j=1}^9 dE_{meas}^{EM_j} \end{aligned} \quad (11)$$

499 We then define the “reduced” p-value according to Eq. (8) using the reduced
 500 \mathcal{L}'_p . This p-value quantifies how frequently a set of particles with true momenta
 501 \vec{p}^0 can produce a set of measurements equally or less probable than the one
 502 observed in data. The p-value is sensitive to inconsistencies in the available
 503 calorimeter measurements and can be used to detect mistakes in the initial
 504 particle content hypothesis. Figure 5(a) shows the distribution of the reduced
 505 p-value for all reconstructed hadronic tau jets in the sample of simulated $Z \rightarrow \tau\tau$
 506 events. The p-value is plotted as a function of the relative difference between the
 507 reconstructed visible tau jet energy at the maximum of the likelihood function
 508 and the true visible jet energy obtained at the particle generator level. It is
 509 evident that a vast majority of mismeasured jets have very low reduced p-value.

510 As it will be shown next, most of these mismeasurements owe to the incorrect
 511 initial particle hypothesis.

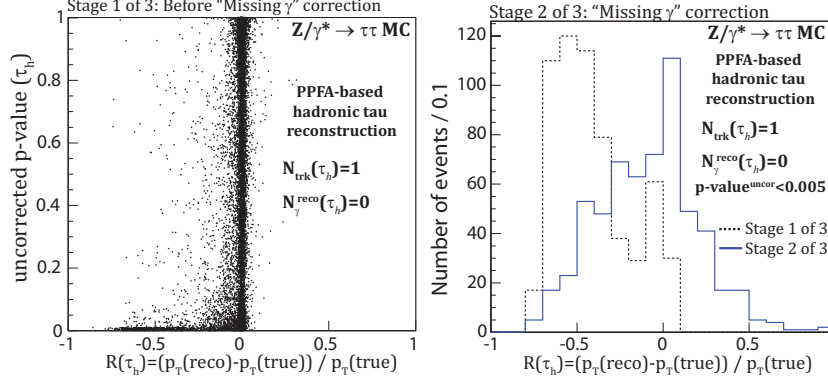


Figure 5: $Z \rightarrow \tau\tau$ events in CDF II detector simulation: 1-prong taus with no photon candidate reconstructed by CES. Left: p-value versus relative energy mismeasurement $R(\tau_h)$. Right: $R(\tau_h)$ for events with small p-value before correction (dashed black line) and after correction for missing photon (solid blue line). As points in the enhancements near the x-axis have typically very low p-values (10^{-3} or less), coarser y-axis binning is chosen to keep these enhancements visible.

512 4.6. Corrections to the Particle Content Hypothesis

513 Based on the simulation studies, the majority of mismeasurements owing
 514 to the incorrect initial particle hypothesis fall into two categories. The first
 515 category includes tau jets with one charged pion and typically one π^0 , where
 516 none of the photons were reconstructed in the CES. This can happen for one
 517 of the following three reasons: (i) a simple CES reconstruction failure (either
 518 dead channels or a photon mostly properly registering in the EM calorimeter but
 519 landing outside the fiducial volume of CES), (ii) the CES cluster is vetoed due to
 520 being too close to the extrapolated track position, or (iii) photon(s) falling into
 521 the uninstrumented regions (“cracks”) between the calorimeter ϕ -wedges. The
 522 last case is likely to be impossible to correct as the deposited electromagnetic
 523 energy is highly sensitive to small differences in the electromagnetic shower

524 development. In addition, photons hitting the cracks may deposit a substantial
 525 portion of their energy in the hadron calorimeter. All three cases lead to a
 526 substantial underestimation of the tau jet energy as only the momentum of the
 527 track would count towards the measurement. To correct for this effect we apply
 528 the following procedure: if a tau candidate with a single reconstructed track and
 529 no reconstructed photons has the reduced p-value that is too small ($p < 0.005$),
 530 we first attempt to correct it by introducing an additional photon. As no CES
 531 measurement is available for this photon, the term with \mathcal{P}^{CES} in Eq.(9) is
 532 removed and the likelihood function with modified particle hypothesis $\mathcal{L}(p_\pi, p_\gamma)$
 533 (or the corresponding \mathcal{L}_E) is recalculated. The new energy is taken as the
 534 updated energy of the tau jet. Figure 5(b) shows the relative difference between
 535 the reconstructed and the true values of the jet energy for these jets before and
 536 after the correction. While the improvement is evident, the catastrophic cases
 537 where photons hit the cracks between the calorimeter wedges cannot be fully
 538 recovered and contribute to reduced resolution. Another contribution, which
 539 makes the distribution broader, comes from events in the second category which
 540 are discussed next and can be corrected.

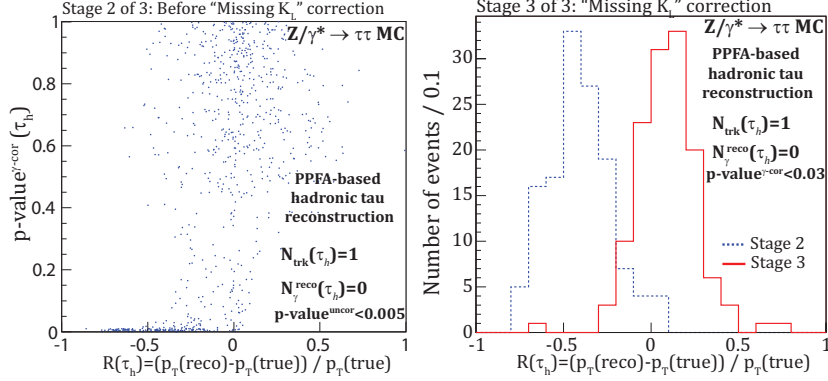


Figure 6: $Z \rightarrow \tau\tau$ events in CDF II detector simulation: 1-prong taus with no photon candidate reconstructed by CES and $p\text{-value}^{\text{uncor}} < 0.005$. Left: p-value after photon correction versus $R(\tau_h)$. Right: $R(\tau_h)$ for events with small $p\text{-value}^{\gamma\text{-cor}}$ before kaon correction (dashed blue line) and after correction for kaons (solid red line).

541 Tau jets with one charged hadron and a stable neutral hadron (kaon), which
 542 is not included in the initial particle content hypothesis, typically have an excess
 543 of energy measured in the hadron calorimeter compared to what one would ex-
 544 pect from a single charged pion. As the excessive energy in the hadron calorime-
 545 ter detected using the p-value cannot be accounted for by adding a photon at the
 546 previous step, the p-value for these jets remains small after an attempted correc-
 547 tion of the initial particle content hypothesis, as shown in Fig. 6(a). Therefore,
 548 for jets with exactly one reconstructed track and no reconstructed photons that
 549 had a low initial p-value ($p < 0.005$) and continue to have a low p-value after the
 550 photon correction (the threshold is $p < 0.03$), the particle content hypothesis is
 551 modified to contain one charged pion and one neutral kaon. Technically, it is ac-
 552 complished by adding a term $\mathcal{P}_n^{CAL}(E^{EM}, E^{HAD}|p_n) = \mathcal{P}_\pi^{CAL}(E^{EM}, E^{HAD}|p_n)$
 553 (as the calorimeter response for charged pions and neutral hadrons is very sim-
 554 ilar) in Eq.(9), and adjusting the argument of the delta-functions to include a
 555 new particle. The energy of the tau jet candidate is updated with the energy
 556 obtained from maximizing $\mathcal{L}_p(p_\pi, p_n)$ (or the corresponding \mathcal{L}_E). The relative
 557 difference between the reconstructed and the true tau jet energy before and
 558 after the correction for this class of jets is shown in Fig. 6(b).

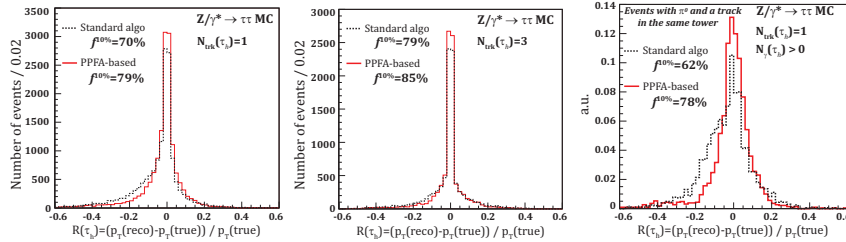


Figure 7: Comparison between reconstructed transverse momentum and true transverse momentum of the hadronic tau for $Z \rightarrow \tau\tau$ events in CDF II detector simulation. The red solid line corresponds to the likelihood method, the black dashed line corresponds to standard CDF tau reconstruction. (a): events with 1-prong tau; (b): events with 3-prong tau; (c): events with significant energy overlap where 1-prong tau is required to have a track and at least one reconstructed CES cluster in the same calorimeter tower.

559 While our procedure has been tuned to improve the overall energy resolution
 560 and not necessarily to reconstruct and identify each individual particle in the
 561 most optimal fashion, we analyze the same sample of simulated $Z \rightarrow \tau\tau$ events
 562 with minimal reconstruction requirements to assess whether the K_L^0 correction
 563 implemented in the algorithm performs as expected. We find that among the
 564 hadronically decaying tau candidates, for which the K_L^0 correction has been in-
 565 voked by our procedure, about 80% of the candidates indeed contain a genuine
 566 K_L^0 in the tau decay chain based on the generator level information. In the re-
 567 maining 20% of the cases, the application of the correction has been triggered by
 568 either significant fluctuations in the hadron showering detected by the algorithm,
 569 or due to various rare mistakes in the baseline tau candidate reconstruction.
 570 Some of these mistakes, e.g. significant track momentum mismeasurements,
 571 happen very rarely, but the K_L^0 correction is capable of detecting at least some
 572 of these cases. In such events, the K_L^0 correction actually improves the overall
 573 jet energy resolution, albeit for the wrong reasons. Note that in our procedure,
 574 the K_L^0 correction is only applied to tau jet candidates with exactly one recon-
 575 structed charged particle track and no reconstructed photon candidates, as this
 576 configuration is the most prone to significant energy mismeasurements due to
 577 late showering energetic K_L^0 's. We find that of all tau candidates with a genuine
 578 K_L^0 falling into this category, in 60% of the cases either a “missing photon” or
 579 “missing kaon” correction is applied in our procedure. Of these cases, about 75%
 580 of the time the p-value reaches an acceptable value after applying the “missing
 581 photon” correction alone and the “missing kaon” correction is thus not invoked.
 582 In the remaining 25% of the cases, the algorithm applies the “missing kaon” cor-
 583 rection. The sequential application of the corrections used in our procedure is
 584 practical given that in the CDF environment the majority of mismeasurements
 585 happen due to unreconstructed photons (tagged using CES clusters). However,
 586 it is clear that one could further improve individual particle identification with
 587 the already existing PPFA tools. For example, one could make a comparison
 588 of the the p-values after applying each of the two corrections separately and
 589 then make a decision on which one is more appropriate in a particular case.

Nevertheless, we conclude that the performance of the correction procedure in our algorithm is consistent with the expectation.

4.7. PPFA Energy Resolution

Figures 7(a) and (b) show the relative difference between the PPFA reconstructed tau jet transverse momentum and the true visible transverse momentum, obtained at generator level for one and three-prong hadronic tau jets. For comparison, the same plots show the performance of the standard CDF tau reconstruction (see [11] for details) shown as dashed line using the same simulated $Z \rightarrow \tau\tau$ events. It is evident that the PPFA algorithm has been able to converge to the correct energy without resorting to complex ad-hoc corrections used in the standard CDF reconstruction. The improvement is particularly striking in cases with significant energy overlaps, as illustrated in Fig. 7(c), which shows the same distribution, but for one-prong events containing at least one photon pointing to the same calorimeter tower as the track.

To quantify the level of improvement, we use the fraction of jets with the reconstructed energy falling within 10% of the true jet energy, denoted as $f^{10\%}$ in Fig. 7. On average, the PPFA increases $f^{10\%}$ by about 10%. The PPFA jet energy resolution distribution also has a more symmetric shape around the true energy and a reduced tail due to jets with underestimated reconstructed energy. The improvement in the tail behavior is more pronounced for one-prong jets as one-prong taus more frequently contain neutral pions with significant contribution towards the total visible jet energy.

It would have been interesting to quantify the improvement in the confusion term in the energy resolution. However, disentangling the contributions to energy resolution from the confusion in assigning energy is not straightforward in PPFA due to the complex convolution of multiple detector responses, including not only the calorimeters but also the Shower Maximum detector. A qualitative feel for the level of the improvement can be deduced from the distributions shown in Fig. 7. As tau decay products rarely contain K_L^0 's, the shape of the underlying broad distribution beneath the near-gaussian narrow core has a

substantial contribution from the “confusion” cases where the electromagnetic deposition of charged pions was not correctly estimated, leading to relatively large mismeasurements. It also has other non-negligible contributions, for example large non-uniformity effects in the response of the electromagnetic calorimeter near the edges of the towers can lead to substantial mismeasurements in tau jet energy if an energetic photon enters the calorimeter near the edge of the tower. These additional effects do not allow one to unambiguously associate the entire shape of the broad component of these distributions with the confusion term. However, narrowing of this distribution in the PPFA case compared to the standard CDF PF-based tau jet reconstruction is most certainly due to improved treatment of the “confusion prone” cases, e.g. see Fig. 7(c) where the fraction of these potentially difficult events is enhanced by the requirement of a track and a CES cluster in the same tower. Therefore the observed improvement can arguably be taken as a lower bound on the relative improvement in the confusion term in PPFA as compared to the standard CDF technique.

5. PPFA Performance Tests Using CDF Data

While the simulation studies show that the PPFA provides an accurate measurement in a single, self-consistent framework free of complex ad-hoc corrections, it is important to validate the algorithm performance in a realistic analysis setting using actual data. Energy resolution for hadronic tau jets cannot be evaluated directly using data. Unlike the case of $Z \rightarrow ee$ or $Z \rightarrow \mu\mu$ events where lepton momentum resolution can be inferred from the broadness of the dilepton mass spectrum, there is no such “standard candle” for taus at hadron colliders. In the case of $Z \rightarrow \tau\tau$, which is the only fairly clean physics signal enriched with true taus accessible at hadron colliders, the shape of the invariant mass distribution calculated using visible tau decay products is very broad, as partial cancellation of the missing transverse energy \cancel{E}_T associated with momenta of the neutrinos from tau decays precludes reconstructing neutrino momenta. In addition to the improved energy resolution, the PPFA can potentially deliver other

649 advantages, e.g. a better discrimination against QCD multi-jet backgrounds due
 650 to “sharper” shapes of identification variables and the new PPFA specific han-
 651 dles, such as the estimate of the jet energy uncertainty on a jet-by-jet basis and
 652 the p -value. However, as many of these potential improvements are correlated,
 653 disentangling and quantifying each of these potential improvements separately
 654 is not practical. Incidentally, a sample of hadronic taus with purity suitable for
 655 such studies would have insufficient statistics due to very harsh cuts required to
 656 reduce background contamination.

657 Given the above limitations, we validate the PPFA in a realistic data setting
 658 and evaluate its performance as follows. First, we demonstrate that the PPFA-
 659 based tau jet energy measurement in the data is well described by the simulation.
 660 Similarly, we show that the PPFA p -value is well reproduced in the data. Second,
 661 we study the tau jet invariant mass distribution for events with tau decays
 662 dominated by $\tau \rightarrow \rho \nu \rightarrow \pi^+ \pi^0 \nu$ and compare the PPFA-based measurement with
 663 that obtained using standard CDF reconstruction. While such invariant mass
 664 is only moderately sensitive to the jet energy resolution, this test allows an
 665 indirect validation of the PPFA jet energy resolution and a comparison with
 666 the standard CDF reconstruction. Finally, as a qualitative demonstration of the
 667 PPFA potential for enhanced background discrimination, we perform two side-
 668 by-side proto-analyses using similar data selections that rely on discriminators
 669 provided by the PPFA in one case and the standard CDF reconstruction in the
 670 other.

671 *5.1. Validation of the PPFA Reconstruction Using $Z \rightarrow \tau\tau$ Data*

672 We use a fairly clean and well understood sample of $Z \rightarrow \tau\tau$ events collected
 673 by CDF in Run-II in the channel where one tau lepton decays hadronically
 674 ($\tau \rightarrow \tau_h \nu_\tau$) and the other decays to a light lepton ($\tau \rightarrow l \nu_\tau \bar{\nu}_l$ where l stands for
 675 an electron or muon). First, we require a tightly isolated reconstructed muon
 676 or an electron with $20 < p_T < 40$ GeV/c and a hadronic tau jet candidate
 677 selected with loose identification requirements. Second, tau jet candidates are
 678 required to have a seed track with $p_T > 10$ GeV/c; no explicit requirement on

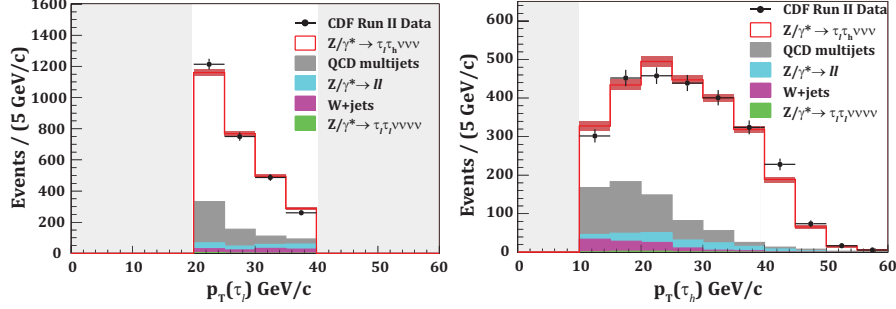


Figure 8: Kinematic distributions demonstrating the purity of the clean tau sample after $Z \rightarrow \tau\tau \rightarrow l\tau_h \nu\nu\bar{\nu}$ ($l = e$ or μ) events are extracted from CDF data with tight selection requirements: (a) transverse momentum of the light lepton, (b) transverse momentum of visible decay products of the hadronically decaying tau lepton, τ_h .

the full momentum of the jet is applied to exclude biases owing to the choice of a tau energy reconstruction algorithm. Following this, several event topology cuts are applied to reduce contamination due to cosmics, $Z/\gamma^* \rightarrow ee$, $Z/\gamma^* \rightarrow \mu\mu$ and W +jets events. A full list of selections is available in [13]. The remaining QCD multi-jet background is estimated from data, using events with lepton and tau candidates having electric charge of the same sign. We rely on simulation to estimate $Z/\gamma^* \rightarrow \tau\tau$, $Z \rightarrow ee$, $Z \rightarrow \mu\mu$ and W +jets contributions. These processes are generated using Pythia Tune A with CTEQ5L parton distribution functions [14] and the detector response is simulated using the GEANT-3 package [9].

Once the sample is selected, the PPFA reconstruction is performed in data and simulation. A thorough comparison of kinematic distributions sensitive to the hadronic tau jet energy measurement has allowed us to conclude that the PPFA performance in the data is well described by the simulation. As an illustration, Figs. 8(a) and (b) show lepton momentum and PPFA-based hadronic tau jet momentum distributions for the selected $Z/\gamma^* \rightarrow \tau\tau$ candidate events to demonstrate the good agreement between data and simulation, as well as to give readers a feel of the purity of the sample used.

As for the new handles made available by the PPFA, we particularly studied

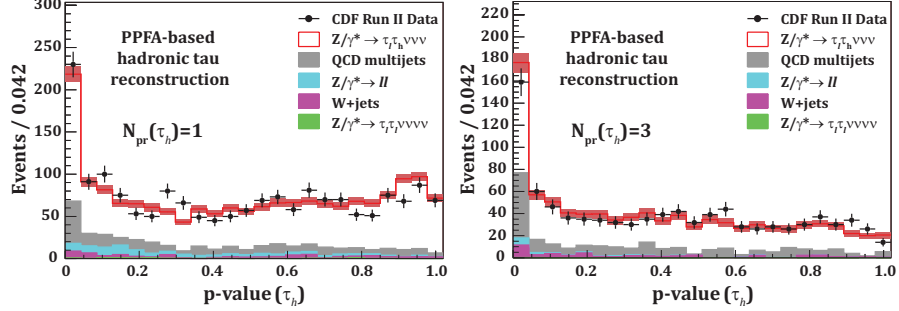


Figure 9: Distribution of hadronic tau candidate p-value for events passing selection requirements in data (points) compared to the sum of background and signal predictions. Left : 1-prong taus. Right: 3-prong taus.

the reduced p -value, which quantifies the level of consistency of the contributing calorimetric measurements with the hypothesis maximizing the PPFA likelihood. Despite its seeming complexity, the distribution for the reduced p -value is well described by the simulation. Figure 9 shows the distribution of the PPFA p -value for selected hadronic tau candidates with one or three charged tracks. Apart from the good agreement between the data and simulation, it is evident that the reduced p -value provides discrimination against the jets from multi-jet QCD events and can be utilized in physics analyses to improve the purity of selected data.

5.2. PPFA Energy Resolution

As discussed earlier, a direct measurement of the energy resolution for hadronic tau jets using data is not possible as the presence of multiple neutrinos in the event precludes reconstruction of the Z boson mass. Conventional estimators performing partial reconstruction of the mass, e.g. the transverse mass of the lepton, hadronic tau jet and the missing transverse energy, all result in broad shapes owing to the unreconstructed neutrinos. The width of these distributions is nearly independent of the tau jet energy resolution⁸, precluding quantitative

⁸Even in more advanced approaches designed to improve mass reconstruction for ditau resonances, e.g. the MMC technique [13], the resolution is still dominated by the accuracy of

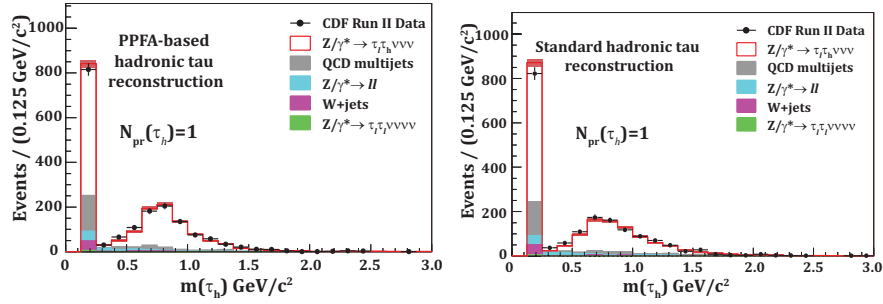


Figure 10: Distribution of the invariant mass for reconstructed hadronic tau candidates in the clean $Z \rightarrow \tau\tau \rightarrow l\tau_h \nu\nu\bar{\nu}$ ($l = e$ or μ) sample extracted from CDF data using tight selection requirements: comparison between PPFA reconstruction (a) and standard CDF reconstruction (b) for all 1-prong tau candidates.

estimations of the latter from data.

Although only modestly sensitive to the accuracy of the jet energy measurement, the reconstructed invariant mass of the constituents of a tau jet can be used for qualitative comparisons. In particular, a significant fraction of one-prong tau jets is produced in decays $\tau_h^\pm \rightarrow \nu_\tau \rho^\pm(770) \rightarrow \nu_\tau \pi^\pm \pi^0$. In these decays, the invariant mass of the hadronic tau jet should be consistent with the mass of ρ -meson and the width of the distribution is sensitive (although somewhat weakly) to the resolution of the hadronic tau jet energy measurement. Figures 10(a) and (b) show distributions of the invariant mass of the one prong tau candidates reconstructed in the data using the PPFA approach and the standard CDF tau reconstruction, with the simulation predictions overlaid. Note that the pedestal near $m = 0.14$ GeV/ c^2 is due to tau jets with no reconstructed photons, which includes π^0 -less one-prong tau decays as well as the cases with the photon being unreconstructed. While these comparisons do not allow quantifying the improvement in the jet energy measurement resolution, it is evident that the PPFA technique provides a better measurement of the tau invariant mass. Similar improvements can be expected for other measurable

the missing transverse energy measurement.

quantities related to particle and energy flow within a tau jet candidate. As tau identification mainly relies on exploring differences in particle and energy flow properties between narrow tau jets and the broader generic jets from the QCD multi-jet backgrounds, such improvements have a potential of improving rejection of multi-jet backgrounds.

5.3. *Tau Identification and Background Discrimination*

While the primary goal of the PPFA is an accurate jet energy measurement in the high occupancy environment, it also provides additional tools that can be used in physics analyses to improve discrimination against backgrounds. Improved accuracy of the measurements of energy, particle and energy flow properties, as well as the new PPFA-specific handles, such as the p -value or the jet-by-jet energy measurement uncertainty, can all aid in discriminating hadronic tau jets from multi-jet QCD backgrounds. To illustrate this, we model two simple proto-analyses, both aiming to maximize the signal to background ratio for a sample of $Z \rightarrow \tau\tau$ candidate events by exploiting properties of the tau jet candidates. One of the analyses relies on variables calculated using standard CDF reconstruction and the other one relies on the PPFA calculations. Both analyses start with a sample of candidate $Z \rightarrow \tau\tau$ events with the level of background contamination due to the QCD multi-jet events that is typical for physics analyses⁹. Compared to the high purity sample, the “realistic” sample is obtained by loosening isolation and some other tight quality requirements on the lepton leg and removing the requirement on the absence of additional energetic jets in the event. The purity and composition of this sample can be inferred from Fig. 11 showing several kinematic and jet shape variables.

Table 1 describes the selections applied. Momentum thresholds and seed track p_T requirements are chosen to select a sample with an acceptable level

⁹The clean $Z \rightarrow \tau\tau$ sample used so far features extremely tight lepton leg selections designed to achieve a high purity source of hadronic taus. While effective in reducing multi-jet backgrounds, such selections are not typical of physics analyses due to their very low signal efficiency.

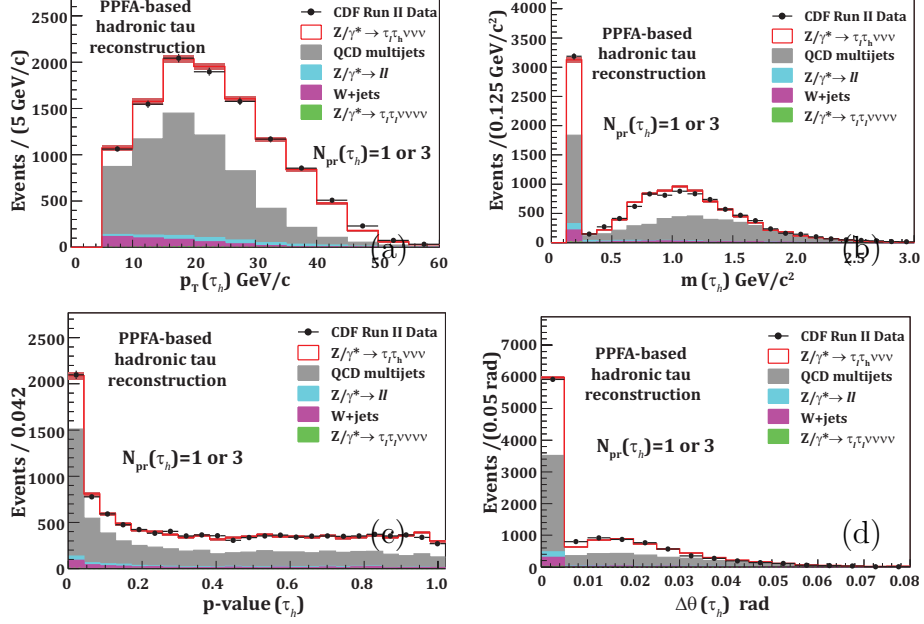


Figure 11: Distributions for the selected 1- and 3-prong tau jet candidates in the sample with enhanced contribution of the QCD multi-jet events. Data (points) compared to the sum of background and signal predictions: (a) transverse momentum of visible decay products (b) hadronic tau visible invariant mass, (c) p-value distribution, (d) $\Delta\theta(\tau)$ distribution.

of background while not being specific to either the PPFA or the standard CDF reconstruction. $N_{iso\ cone}^{trk}$ is the number of tracks with $p_T > 1$ GeV/c in the isolation cone. $\Delta\theta(\tau) = \sum E_i \times \theta_i / \sum E_i$ is the weighted angular width of the jet calculated using the momenta of individual particles reconstructed in a jet, similar to the case of the previously discussed jet invariant mass $m(\tau)$. The summation goes over particles in the jet, E_i being the particle energy and θ_i is the angle between the particle and the visible 4-momentum of the tau jet. The specific cut choices for $\Delta\theta(\tau)$ and $m(\tau)$ (see Table 1) aim at a high signal efficiency while rejecting the tails of the corresponding distributions dominated by the background events. These cuts are therefore expected to reduce background contamination, but are not optimized in any particular way. The selections discussed above can be equally applied to both the standard and the PPFA-based analyses. Finally, we apply an additional p_T -dependent cut

Table 1: Selections used in the two proto-analyses using either PPFA or standard CDF selection for hadronically decaying tau jets. The first group of selections corresponds to standard CDF selections applied first in both analyses. The second group shows additional non-standard selections using the invariant mass and the narrowness of the tau candidate’s jet cluster that can be applied to both analyses. The last selection uses the PPFA p-value and is only applied to the PPFA proto-analysis.

1-prong	3-prong
$p_T > 10 \text{ GeV}/c$	$p_T > 15 \text{ GeV}/c$
$p_T^{seed \text{ trk}} > 10 \text{ GeV}/c$	$p_T^{seed \text{ trk}} > 10 \text{ GeV}/c$
$N_{iso \text{ cone}}^{trk} = 0$	$N_{iso \text{ cone}}^{trk} = 0$
$0 < m(\tau) < 0.25 \text{ or}$ $0.375 < m(\tau) < 1.4 \text{ GeV}/c^2$	$0.8 < m(\tau) < 1.4 \text{ GeV}/c^2$
$\Delta\theta < 0.04$	$\Delta\theta < 0.015$
Only the PPFA-based analysis:	
$p > 0.008 \text{ if } p_T < 20 \text{ GeV}/c$	$p > 0.06 \text{ if } p_T < 30 \text{ GeV}/c$

on the p -value in the PPFA-based analysis only. The distributions for these variables using PPFA definitions are illustrated in Figs. 11(b), (c) and (d).

To compare the default reconstruction and PPFA side-to-side, Figs. 12(a) and (b) show the “after” distributions for $m(l, \tau, \cancel{E}_T)$, the visible mass of lepton, tau and missing transverse energy¹⁰, for each of the two proto-analyses. As a quantitative figure of merit for the comparison of the two techniques, in Fig. 12(c) we show the ratio $N^{Z \rightarrow \tau\tau}(m > m_0)/N^{QCD}(m > m_0)$, where $N^{Z \rightarrow \tau\tau}(m > m_0)$ and $N^{QCD}(m > m_0)$ are the estimated rates of events and background events with $m(l, \tau_h, \cancel{E}_T) > m_0$, for the selected sample as a function of m_0 . Note that backgrounds are heavily dominated by the QCD multi-jet events. Near its maximum, the S/B ratio is a factor of 1.7 higher for the PPFA case. While by no means exhaustive, this comparison indicates the potential of

¹⁰This quantity is frequently used as the final discriminant in physics analyses [5, 15]

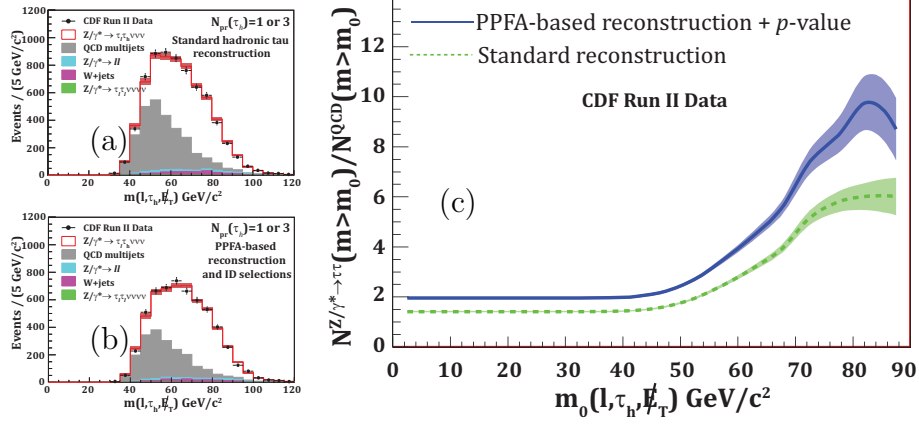


Figure 12: The distribution of the visible mass, $m(\tau, l, \cancel{E}_T)$ for events with 1 and 3-prong taus in data (points) compared to the sum of background and signal ($Z \rightarrow \tau\tau$) predictions after applying selections utilizing variables calculated using either standard CDF reconstruction (a), or PPFA (b). The PPFA case includes a cut on the p-value and otherwise the cut values are the same. (c) S/B ratio as a function of minimal threshold m_0 on $m(\tau, l, \cancel{E}_T)$. The dashed (green) line shows the standard CDF tau reconstruction and the solid (blue) line corresponds to PPFA; bands indicate the statistical uncertainty on the ratio due to the size of the sample and fluctuations in background contributions.

the PPFA technique in discriminating hadronic tau jets from quark and gluon jets, thus providing a nice byproduct of the method that can be utilized in physics analyses.

6. Conclusions

The PPFA is a consistent, probabilistic framework designed for accurate reconstruction of the jet energy in the high occupancy environment, relevant for experiments operating in the very high luminosity regime or featuring coarse calorimeter segmentation. The framework is based on “first principles” and is essentially free of ad-hoc corrections. The PPFA can be implemented in a realistic detector setting, as demonstrated using the example of hadronic tau reconstruction at CDF. It is shown to provide a more accurate jet energy measurement and better discrimination against backgrounds compared to the existing tools utilizing the particle flow concept. For hadronic tau reconstruction, the

new tools provided by the PPFA, such as a jet-by-jet estimate of the jet energy uncertainty and the p -value quantifying the likelihood of the current hypothesis about particle content of a jet, can be used to further improve energy resolution and provide better discrimination against backgrounds. The proposed technique can be utilized at the LHC experiments once the machine is upgraded for the very high luminosity regime as well as at future collider experiments.

Acknowledgments

We thank Anthony K. Rose, Robert M. Roser, and Jeffrey K. Roe for carefully reading the manuscript and their useful suggestions. We thank our CDF collaborators for their support and the Fermi National Accelerator Laboratory, where a part of the work on the paper has been performed. This work would not be possible without the funding support of the U.S. Department of Energy, the DOE OJI program, and the State of Texas.

References

- [1] M. A. Thomson arXiv:0709.1360.
- [2] D. Buskulic *et al.*, (ALEPH Collaboration), Nucl. Instrum. Methods A **360**, 481 (1995).
- [3] J. C. Brient and H. Videau, arXiv:hep-ex/0202004v1 (2002).
- [4] A. Connolly, Report No. FERMILAB-THESIS-2003-45, 2003.
- [5] A. Abulencia *et al.* (CDF Collaboration), Phys. Rev. D **75**, 092004 (2007).
- [6] A. Bocci, S. Lami, S. Kuhlmann, G. Latino, Int. J. Mod. Phys. A16 S1A, 255 (2001).
- [7] CMS Collaboration, Report No. CMS-PAS-PFT-08-001, 2008.
- [8] A. Abulencia *et al.* (CDF Collaboration), J. Phys. G 34, 2457 (2007);
D. Acosta *et al.* (CDF Collaboration), Phys. Rev. D **71**, 032001 (2005).

- 821 [9] R. Brun, R. Hagelberg, M. Hansroul and J.C. Lassalle, CERN-DD-78-2-
822 REV.
- 823 [10] T. Sjostrand, P. Eden, C. Friberg, L. Lonnblad, G. Miu, S. Mrenna, and
824 E. Norrbin, Comput. Phys. Commun.**135**, 238 (2001).
- 825 [11] A. Abulencia *et al.* (CDF Collaboration), Phys. Rev. D**75**, 092004 (2007).
- 826 [12] A. Bhatti *et al.*, Nucl. Instrum. Methods A**566**, 375-412 (2006).
- 827 [13] A. Elagin, P. Murat, A. Pronko, and A. Safonov, Nucl. Instrum. Methods
828 A**654**, 481-489 (2011).
- 829 [14] H.L. Lai *et al.*, Eur. Phys. J. C**12**, 375 (2000).
- 830 [15] A. Aaltonen *et al.* (CDF Collaboration), Phys. Rev. Lett.**103**, 201801
831 (2009).